Polymer-Controlled Growth Rate of an Amorphous Mineral Film Nucleated at a Fatty Acid Monolayer

E. DiMasi*

Physics Department, Brookhaven National Laboratory, Building 510B, Upton, New York 11973-5000

V. M. Patel, M. Sivakumar, M. J. Olszta, Y. P. Yang, and L. B. Gower

Department of Materials Science and Engineering, University of Florida, 210A Rhines Hall, P. O. Box 116400, Gainesville, Florida 32611-6400

Received May 28, 2002. In Final Form: August 26, 2002

The nucleation and growth rate of an amorphous mineral film at a Langmuir monolayer interface has been observed in situ with X-ray scattering techniques for the first time. We present measurements of a calcium carbonate film, nucleating at a fatty acid monolayer from a supersaturated calcium carbonate subphase containing a dilute poly(acrylic acid) additive, in emulation of biogenic mineralizing systems. The arachidic acid molecules were observed to self-assemble on the subphase into an untilted structure, with one bound Ca^{2+} ion per 14−25 surfactant molecules, and with a two-molecule planar centered rectangular unit cell with lattice constants $a = 4.38$ Å and $b = 8.51$ Å. Subsequently, an amorphous mineral phase forms beneath the monolayer, growing at a rate of 22 Å/h to a thickness of 300 Å after about 15 h. The electron density of the film was 0.7 times that of crystalline calcium carbonate hexahydrate, suggesting that the precursor is a hydrated phase with an open structure. During film growth, no changes were observed in the in-plane scattering peaks from the arachidic acid monolayer. No intensity was observed at Bragg peak positions for anhydrous calcium carbonate minerals. These observations indicate that nucleation of the calcium carbonate film is not directed by atomic scale templating at the fatty acid, but is instead dictated by the redistribution of ions near the interface. We discuss the relevance of our study to template-directed nucleation in the contexts of biomineralization and biomimetic materials science.

I. Introduction

In the process of biomineralization, a living organism provides a chemical and physical environment that directs the growth of minerals into precisely controlled morphologies and polytypes. One of the persistent questions that arises in trying to understand these structures concerns the effects of organic molecules involved in biomineralization, and a distinction is generally made between soluble and insoluble organic materials, which are believed to play somewhat different roles.[1] In a number of biogenic minerals, an insoluble organic matrix provides an obvious structural scaffold (for example, collagen in bone). When this kind of organic matrix has atomic-scale features that exhibit good registry with the lattice sites in the adjacent mineral, it is natural to suggest that the organic also acts as a template to direct preferential nucleation of a particular crystal face.[2] The design of ceramics and composite materials certainly stands to benefit from a better understanding of how this kind of template control can be used to advantage.

A large number of biomineral-inspired in vitro studies have therefore been pursued, to try to clarify the mechanisms of template-directed mineralization. One promising approach to mineralization at an organic template involves the nucleation of minerals from solution onto surfactant layers on solid or liquid substrates. Under the right conditions, the monolayer films self-assemble into simple, well-understood two-dimensional structures. With the right choice of surfactant, the variation of intermolecular distances, surface charges, and so on can be systematically studied. The potential for mineralization at tunable surfactant monolayers assembled at the liquid surface has been demonstrated in the study of calcium carbonate nucleation, where calcite or vaterite crystals having specific size distributions, habits, and orientations at the surface were grown.[3−6] In the wake of these experiments, template-directed nucleation is being pursued in a variety of other systems, and at the present time, the importance of an atomic-scale template is essentially taken for granted. Crystallization driven by various monolayer templates assembled at liquid interfaces has been described for barium and copper sulfates,[7−12] potassium dihydrogen phosphate,[13] barium fluoride,[14] and

* Corresponding author. E-mail: dimasi@bnl.gov.

(1) Lowenstam, H. A.; Weiner, S. *On Biomineralization*; Oxford University Press: New York, 1989.
(2) Buijnsters, P. J. J. A.; Donners, J. J. J. M.; Hill, S. J.; Heywood, B. R.; Nolte, R. J. M.; Zwanenburg, B.; Sommerdijk, N. A. J. M. *Langmuir* **2001**, *17*, 3623.
(3) Mann, S.; Heywood, B. R.; Rajam, S.; Birchall, J. D. *Nature* **1988**, *334*, 692.
(4) Mann, S.; Heywood, B. R.; Rajam, S.; Birchall, J. D. *Proc. R. Soc., London* **1989**, *A423*, 457.
(5) Rajam, S.; Heywood, B. R.; Walker, J. B. A.; Mann, S. *J. Chem. Soc., Faraday Trans.* **1991**, *87*, 727.
(6) Heywood, B. R.; Rajam, S.; Mann, S. *J. Chem. Soc., Faraday Trans.* **1991**, *87*, 735.
(7) Heywood, B. R.; Mann, S. *J. Am. Chem. Soc.* **1992**, *114*, 4681.
(8) Heywood, B. R.; Mann, S. *Langmuir* **1992**, *8*, 1492.
(9) Tang, R.; Tai, Z.; Chao, Y. *J. Chem. Soc., Dalton Trans.* **1996**, 4439.
(10) Tang, R.; Tai, Z.; Chao, Y. *Chem. Lett.* **1996**, 535.
(11) Tang, R.; Jiang, C.; Tai, Z. *J. Chem. Soc., Faraday Trans.* **1997**, *93*, 3371.
(12) Tang, R.; Jiang, C.; Tai, Z. *J. Chem. Soc., Dalton Trans.* **1997**, 4037.
(13) Li, B.; Liu, Y.; Yu, J.; Bai, Y.; Pang, W.; Xu, R. *Langmuir* **1999**, *15*, 4837.
(14) Lu, L.; Cui, H.; Lei, W.; Zhang, H.; Xi, S. *Chem. Mater.* **2001**, *13*, 325.

10.1021/la0260032 CCC: $22.00
Published on Web 10/10/2002

layered double hydroxide minerals,[15] to give only a partial survey (and to leave aside the many related studies on solid substrates).

Many of the above cited works offer explanations primarily in terms of the registry between the two-dimensional template structure and the atomic positions in the crystal face grown against the template. Other mechanisms acknowledged to be important are the ability of a template to provide a boundary surface, to collect cations from solution, and to otherwise affect the local chemistry that determines the kinetics of mineralization.[16] In this context, it is important to remember that a number of biominerals are in fact amorphous. Even in the case of calcium carbonates, where the hydrated amorphous phase is not stable under uncontrolled environmental conditions, a number of organisms either stabilize amorphous hydrated calcium carbonates in their bodies,[17] or exhibit crystalline $CaCO_3$ structures that develop through a short-lived amorphous precursor phase.[18] An explanation for stability and control of the amorphous systems is believed to lie in the *soluble* acidic macromolecules present during biomineralization, which are known under some conditions to inhibit crystal nucleation and growth.[1] Here the importance of atomic-scale registry with a template is called into question, although the template may become important if the amorphous phase subsequently crystallizes.

Amorphous mineralizing systems may offer a simplification, then, in separating the effects of template versus kinetic control of mineralization, and a number of model systems have been pursued here as well. In the case of calcium carbonates, conditions have been identified that either force mineralization to proceed via amorphous precursor phases,[19,20] or that can stabilize $CaCO_3$ in amorphous form.[21] Incorporation of carbonate ions into amorphous calcium phosphate films has also been shown to delay conversion to the crystalline phase.[22] In these studies as in nature, soluble organic species along with an insoluble boundary surface are present. Despite the temptation to understand the organic species in terms of these two categories, they are likely in reality to play overlapping roles in controlling mineralization kinetics. To understand how this occurs, new experimental techniques must be applied to these model systems. In the works cited above, concerning both crystalline and amorphous materials, mineral polytype and morphology were assessed by optical and electron microscopy and ex situ diffraction techniques. These observations are not sensitive to the microscopic arrangements of surfactant molecules and cations, nor can they directly measure crystal growth during its earliest stages. Serious difficulties in interpretation result: for example, pressure−area isotherms of surfactants spread on the mineralizing subphase often indicate that the phase behavior is completely different from that obtained on a pure water subphase. Yet the structures of the resulting mineral faces grown against the template were only compared to the nominal surfactant structures as assembled on pure water. In situ structural measurements on atomic length scales are badly needed to provide information about the nucleation and crystallization of these systems.

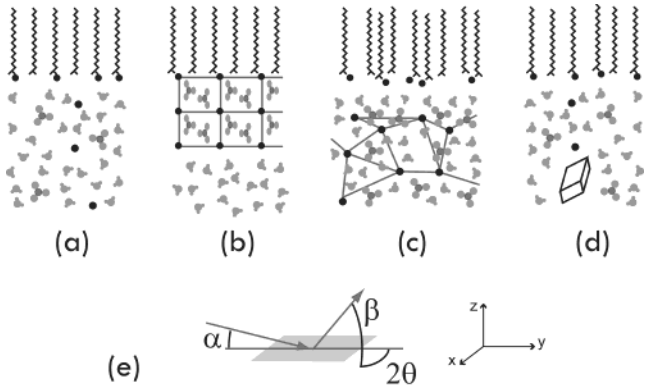

Figure 1. (a) Schemes for mineralization from solution at a Langmuir film interface. As the first stage of nucleation at a monolayer film, the anionic headgroups are expected to attract a layer of bound cations, which can affect the cation supersaturation in the vicinity of the monolayer. (b) When there is good registry between the lattice spacings of the surfactant and the mineral, template-directed mineralization may occur. (c) An alternative route to mineralization is via a hydrated amorphous precursor which forms in the region of altered chemical composition at the interface. (d) Experiments must also distinguish the process of homogeneous nucleation in solution, where macroscopic crystals form independently of the monolayer template. (e) Geometry for X-ray scattering from a self-assembled monolayer film. The momentum transfer $\mathbf{q} = \mathbf{k}_{out} - \mathbf{k}_{in}$ is a function of the incident angle α, reflected angle β, and in-plane scattering angle 2θ.

To illustrate the above points, we consider possible routes to mineralization for a calcium carbonate/fatty acid monolayer assembled on an aqueous subphase, as depicted in Figure 1a−d. First, it is expected that the charged headgroups will attract a layer of calcium cations from the solution (Figure 1a). If the lattice spacings of the surfactant and mineral structures match closely, discrete crystals or a thin crystalline layer may form directly at the template interface (Figure 1b). This model, previously proposed for such a system,[3] presumes a high concentration of ordered cations at the interface. On the other hand, the monolayer may not interact this strongly with the nucleating minerals. It may instead simply change the local supersaturation by binding cations, or perhaps just form a physical boundary that collects the mineral constituents, which may then nucleate and later crystallize through a route involving metastable hydrated and/or amorphous phases (Figure 1c). We must also be prepared for the outcome shown in Figure 1d, where homogeneous nucleation in the bulk subphase leads to crystals that may collect at the surface but have not nucleated near the monolayer. In principle, all of these cases can result in similar distributions of macroscopic crystals *or* extended thin films, and all of these conditions may involve changes to the "native" two-dimensional ordering of the surfactant molecules.

Synchrotron X-ray scattering can provide the needed structural information to distinguish unequivocally between these very different mineralization schemes. X-ray scattering is of course a long-used probe for the study of film structures. More recently, synchrotron sources have allowed in situ X-ray reflectivity and grazing incidence diffraction to be conducted at liquid surfaces.[23] The

(15) He, J. X.; Yamashita, S.; Jones, W.; Yamagishi, A. *Langmuir* **2002**, *18*, 1580.
(16) Kraus, B. L.; Crenshaw, M. A. *Chem. Geol.* **1996**, *132*, 183.
(17) Levi-Kalisman, Y.; Raz, S.; Weiner, S.; Addadi, L.; Sagi, I. *J. Chem. Soc., Dalton Trans.* **2000**, 3977.
(18) Beniash, E.; Aizenberg, J.; Addadi, L.; Weiner, S. *Proc. R. Soc., London* **1997**, *B*, 461.
(19) Xu, G.; Yao, N.; Aksay, I. A.; Groves, J. T. *J. Am. Chem. Soc.* **1998**, *120*, 11977.
(20) Gower, L. B.; Odom, D. J. *J. Cryst. Growth* **2000**, *210*, 719.
(21) Aizenberg, J.; Lambert, G.; Weiner, S.; Addadi, L. *J. Am. Chem. Soc.* **2002**, *124*, 32.
(22) Xu, G.; Aksay, I. A.; Groves, J. T. *J. Am. Chem. Soc.* **2001**, *120*, 2196.
(23) *Synchrotron Radiat. News* **1999**, *93*.

geometry used for these surface scattering experiments is indicated in Figure 1e. With X-rays incident onto the sample at an angle α, intensity can be detected at reflection angle β and in-plane scattering angle 2θ. The momentum transfer components within and normal to the layer plane, which relate these angles to scattered intensity in reciprocal space, are given by

$$q_{xy} = (2\pi/\lambda)[\cos^2\alpha + \cos^2\beta - 2\cos\alpha\cos\beta\cos(2\theta)]^{1/2};$$
$$q_z = (2\pi/\lambda)[\sin\alpha + \sin\beta] \quad (1)$$

respectively.[24] X-ray reflectivity, measured under the conditions $\alpha = \beta$ and $2\theta = 0$, is a sensitive measure of the surface-normal electron density profile at an interface. The grazing-incidence technique, with α constrained to be smaller than the angle for total external reflection of X-rays, is used to detect in-plane diffraction peaks at scattering angle 2θ from structures within a few tens of angstroms of the surface, while reducing the background scattering from the bulk subphase. By combining the two complementary X-ray measurements, the sub-angstrom scale structure of a film along the surface normal can be determined, and in-plane crystalline order can be detected. In the past 15+ years, such liquid surface X-ray techniques have revealed a wealth of information on the structural phases of surfactants.[25]

It is surprising that these techniques have not really been brought to bear on biomineralizing interfaces, considering the many debates that arise concerning the crystallinity and molecular conformations of the nucleating minerals. To our knowledge, the most closely related recent scattering studies in this area involve surfactant-induced nucleation of silica/organic laminates,[26−28] and nucleation of barium fluoride species at fatty acids.[29] It is desirable to understand the mechanisms of biomineralization, operating at the interface between organic molecules and nucleating crystals, by pinpointing the transformation between the disordered aggregate of assembled molecules and the macroscopic crystal. With X-ray reflectivity one can in principle determine the structure, thickness, and composition of these atomic-scale precursors to mineral nucleation. In combination with grazing incidence diffraction, the time-dependent domain size, crystallinity, and orientation of the minerals as well as the surfactant can be directly studied.

In the present paper we demonstrate the use of synchrotron X-ray scattering to study biomimetic mineral growth at surfactant/ion/liquid interfaces. We present the first synchrotron X-ray observations of the growth of a calcium carbonate mineral, from its inception as a collection of cations at a fatty acid monolayer interface, to a macroscopic mineral film. To make the film, an arachidic acid monolayer was prepared on a supersaturated calcium carbonate subphase containing a dilute poly(acrylic acid) additive, in emulation of biogenic mineralizing systems, which contain soluble acidic polymers. (We have found that poly(acrylic acid) and poly(aspartic acid) behave in a very similar fashion with respect to the deposition of mineral films.[30]) The arachidic acid molecules were observed to self-assemble on the subphase into an untilted structure, with one bound Ca^{2+} ion per 14−25 surfactant molecules. Subsequently, an amorphous mineral phase was observed, growing at a rate of 22 Å/h to a thickness of 300 Å after about 15 h. The electron density of the film was 0.7 times that of calcium carbonate hexahydrate, suggesting that the precursor is a more hydrated phase with an open structure. During film growth, no changes were observed in the in-plane scattering peaks from the arachidic acid monolayer. These observations indicate that nucleation of the calcium carbonate film is not directed by atomic-scale templating at the fatty acid, but is directed by solution kinetics instead.

II. Experimental Details

A supersaturated calcium carbonate solution was prepared by dissolving calcium carbonate powder (ground from single-crystal calcite pieces) in purified water (2 g of $CaCO_3$/800 mL of MilliRho 18 MΩ).[31,32] Carbon dioxide gas was bubbled into the solution through a coarse glass frit, while stirring with a Teflon-coated magnet on a stirring plate for 24 h. The solution was filtered (Whatman no. 3 paper), bubbled with CO_2 again for an hour, and refiltered. The weight of undissolved calcium carbonate powder on the first filter cake gives an upper bound of about 10 mM $CaCO_3$ concentration for the solution. Poly(acrylic acid, sodium salt), molecular weight 8000, was obtained as a 45 wt % stock solution from Aldrich, diluted with water, and added to the carbonate subphase to a final concentration of 32 μg/mL.

The subphase was poured into a Langmuir trough equipped with a computer-controlled barrier and pressure balance with a Wilhelmy plate cut from clean filter paper. The balance was calibrated using an 18 mg metal weight. The arachidic acid monolayer was spread from chloroform solution. After sample preparation, the trough was closed within a gastight box to allow the X-ray measurements to be made under a flowing helium atmosphere. A chiller unit maintained a bath temperature of 19 °C. The trough is 40 cm long along the direction of barrier travel, 16 cm wide, and 0.6 cm deep. To reduce surface waves, a glass plate 0.5 cm thick is placed in the trough in the region of the beam path. These details are important to note since the dimensions of the trough affect the rate at which carbon dioxide gas escapes from the water, changing the supersaturation of the solution and the pH, affecting the mineralization rate. In principle the presence of hydrated helium gas rather than air above the sample may also affect the CO_2 escape rate slightly. Separate experiments on the benchtop have confirmed that air and helium atmospheres have the same qualitative results for film growth. In the absence of soluble polymers, we reproduce the results reported in the literature for calcium carbonate nucleation at fatty acid monolayers, whether in helium or in air.[33]

The experiments utilized the Harvard/BNL liquid surface spectrometer at beamline X22B at the National Synchrotron Light Source at Brookhaven National Laboratory. Reflectivity measurements were made with a Bicron single channel detector, with resolution $\approx$0.007 Å^{-1} defined by 2 mm × 2 mm slits approximately 600 mm from the sample, using an X-ray wavelength of 1.556 Å. The background scattering from the bulk solution, subtracted from the specular signal, was measured with the detector displaced out of the reflection plane. Grazing incidence diffraction measurements were performed at an incident X-ray angle of 0.12°. The scattered intensity was resolved in the outgoing angle using a vertically oriented linear detector with a 10 cm long active area, and collimated in the horizontal plane by a set of Soller slits with 0.16° acceptance.

(24) Schwartz, D. K.; Schlossman, M. L.; Pershan, P. S. *J. Chem. Phys.* **1992**, *96*, 2356.
(25) Kaganer, V. M.; Möhwald, H.; Dutta, P. *Rev. Mod. Phys.* **1999**, *71*, 779.
(26) Brown, A. S.; Holt, S. A.; Dam, T.; Trau, M.; White, J. W. *Langmuir* **1997**, *13*, 6363.
(27) Brown, A. S.; Holt, S. A.; Reynolds, P. A.; Penfold, J.; White, J. W. *Langmuir* **1998**, *14*, 5532.
(28) Holt, S. A.; Foran, G. J.; White, J. W. *Langmuir* **1999**, *15*, 2540.
(29) Kmetko, J. Unpublished data.
(30) Kim, Y.-Y.; Gower, L. B. Submitted for publication *in MRS Proceedings—Symposium N: Biological and Biomimetic Materials—Properties to Function*.
(31) Kitano, Y. *Bull. Chem. Soc. Jpn.* **1962**, *35*, 1973.
(32) Kitano, Y. *Bull. Chem. Soc. Jpn.* **1962**, *35*, 1980.
(33) DiMasi, E.; Gower, L. B. In *Advanced Biomaterials—Characterization, Tissue Engineering, and Complexity*; The Materials Research Society: Warrendale, PA, 2002; Vol. 711, p 301.

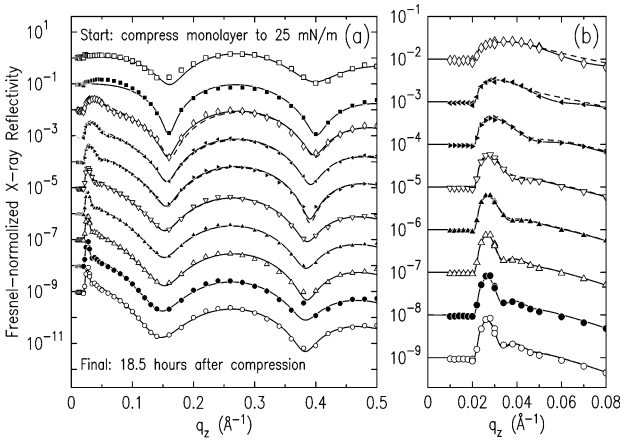

Figure 2. (a) Fresnel-normalized reflectivity data from initial compression of the monolayer (□) and at subsequent times: ■, 1.5 h; ◊, 5.0; left-pointing ▲, 7.5; right-pointing ▲, 8.5; ▽, 11.2; ▲, 12.5; △, 15.2; ●, 17.0; ○, 18.5 h. Curves following the top one are shifted by successive factors of 10 for clarity. (b) Low-q_z region, with same symbols and offsets as in (a). Solid and dashed lines are fits to the data as described in the text.

III. Experimental Results

The reflectivity and grazing incident in-plane measurements were made at intervals of 2−3 h from the time of initial film compression, for a period of 20 h. The time series of reflectivity curves is shown in Figure 2a. The curves are normalized by the calculated Fresnel reflectivity of water, and each curve is shifted by a factor of 10 relative to the previous one, for clarity. The first measurement (□, at top of figure) exhibits minima at $q_z = 0.15$ Å^{-1} and $q_z = 0.41$ Å^{-1}, which result from interference of X-rays reflecting from the air/monolayer and monolayer/water interfaces, which are approximately 24 Å apart. The detailed q_z dependence of the reflectivity provides information on the monolayer structure. Subsequently, an additional interference peak appears at $q_z \approx 0.03$ Å^{-1}, as emphasized in Figure 2b. This sharp peak at low q_z is due to interference from an additional interface which is more than 50 Å from the monolayer interfaces, and indicates that a coherent mineral film has formed beneath the monolayer. From fits of the data to reflectivities calculated from model surface-normal density profiles (solid and dashed lines in Figure 2), the density and thickness of the mineral layer can be determined as a function of time. The reflectivity analysis and quantitative structural models that characterize the thick mineral film will be described in the next section.

The grazing-incidence diffraction measurements provide information about the in-plane structure of the monolayer and mineral film. With the X-ray beam incident into the sample at an angle of 0.12°, the penetration depth of the X-rays is restricted to about 75 Å, probing the near-surface region while minimizing the bulk water background scattering. In-plane diffraction was surveyed in the range $15° \le 2\theta \le 45°$, covering a wide range of Bragg peak positions for known calcium carbonate mineral phases,[34,35] and resolved in β with a position-sensitive detector over the range $0 \le \beta \le 10°$, to detect signatures of preferential orientation of crystals or tilts of the surfactant molecules. The only features observed above the background scattering were a pair of peaks, shown in Figure 3, which we measured at 2−3 h intervals from 4 to 19 h since preparation of the monolayer. The data shown as open circles have been integrated over the full β range, with the angle 2θ converted into the in-plane momentum transfer q_{xy}. (Refer to Figure 1e and eq 1.)

The intensities from both peaks have their maximum at $q_z = 0$, as shown by the insets at the top. The q_z dependence of the intensity, falling to background level at $q_z \approx 0.25$ Å^{-1}, is characteristic of scattering from a layer of thickness $(2\pi/0.25) \approx 25$ Å, in other words, from the surfactant monolayer. The data cannot be described by a thick diffracting film or bulk subphase.

(34) Brooks, R.; Clark, L. M.; Thurston, E. F. *Proc. R. Soc., London* **1950**, *243A*, 145.

(35) Dickens, B.; Brown, W. E. *Inorg. Chem.* **1970**, *9*, 480.

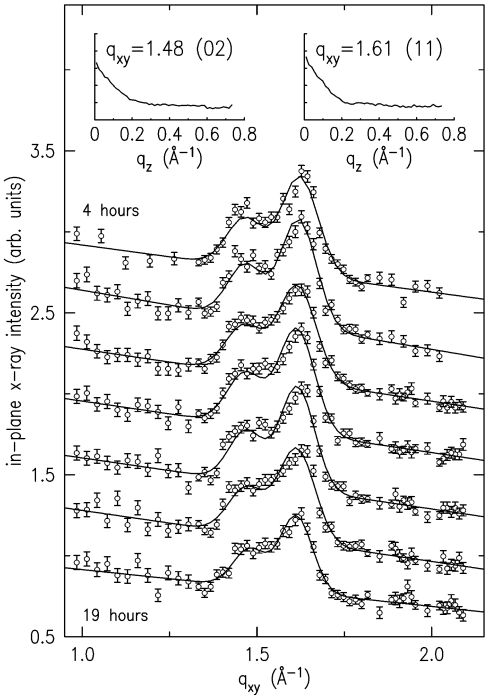

Figure 3. (○) Time series of scattered intensity at grazing incidence, integrated over the reflection angle $0 \le \beta \le 10°$, as a function of in-plane momentum transfer q_{xy}. Gaussian peak fits are shown as solid lines. Insets at top: q_z dependence of scattered intensity, from counts combined from the five latest time scans and averaged over ±0.05 Å^{-1} intervals about the labeled q_{xy} positions. Labels in parentheses show the indices of the two peaks in the centered rectangular unit cell with a two-atom basis.

The in-plane peaks remain unchanged during the course of the experiment, even though the underlying mineral becomes several hundreds of angstroms thick. The in-plane structural order present is therefore characteristic of the arachidic acid monolayer, and not the mineral film.

The peaks can be characterized by a pair of Gaussian curves on a linear background, as shown by solid lines fit to the data in Figure 3. The peaks have positions 1.476 ± 0.010 and 1.614 ± 0.005 Å^{-1}, full widths of 0.11 ± 0.02 (held in fits to be the same for both peaks), and are well described by amplitude ratios close to 1:2. These peaks are very weak and broad in comparison to those which can be obtained from well-ordered surfactant monolayers, for which micron-sized domains are routinely obtained. Here, the broad peaks are indicative of domain sizes on the order of 60 Å, considerably smaller than our resolution limit. This evidence for disruption of the monolayer structure is consistent with the reflectivity analysis to be described in the next section.

We index these peaks as the (02) (weaker peak at 1.476 Å^{-1}) and degenerate (11), (−11) (doubly intense peak at 1.614 Å^{-1}) reflections from a centered rectangular unit cell, which is an established structure for fatty acid monolayers. The fact that the peak intensity is maximum at $q_z = 0$ indicates that the hydrocarbon tails stand up normal to the liquid surface. This model leads to lattice parameters of $a = 4.38$ Å and $b = 8.51$ Å, the average molecular area being 18.63 Å^2 per molecule. In the Discussion section we will make comparisons to known film structures, and address alternative interpretations of the data.

IV. Reflectivity Analysis

Because X-rays scatter primarily from the electrons in a material, the scattered intensity provides information about the spatial variation of electron density, which can then be given a structural interpretation in terms of atomic positions. In the surface geometry used for the present experiments, the reflectivity measurements are interpreted by calculating the reflectivity $R(q_z)$ from a model

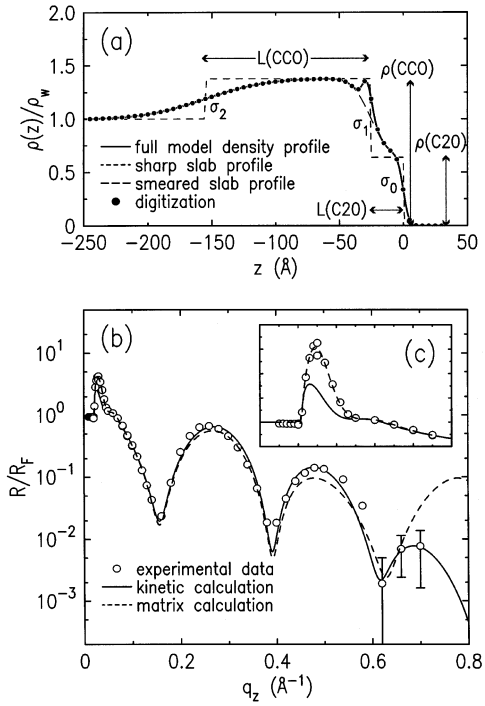

Figure 4. (a) Model density profile constructed from two slabs and a Gaussian, defined by parameters as described in the text. Components of the model are shown separately, as labeled in the figure key. (b) (○) Experimental reflectivity data, normalized by the Fresnel reflectivity, 8.5 h after film compression. (—) Reflectivity calculated from full model shown in (a), using the kinematic approximation and parameters given for this sample in Table 1. (---) Reflectivity calculated using the matrix method and digitized density profile indicated by circles in (a). (c) Normalized reflectivity in the region $0 \le q_z \le 0.1$ Å^{-1}, with symbols as in (b).

surface-normal electron density profile $\rho(z)$, and refining the calculated pattern against the data. In the kinematic limit, which is the regime where the ratio of scattered to incident X-rays is much less than unity, the relationship can be written as

$$R(q_z) = R_F\left|\frac{1}{\rho_w}\int \frac{\partial \rho(z)}{\partial z} e^{-iq_z z}\, dz\right|^2 \qquad (2)$$

In eq 2, the Fresnel reflectivity R_F for water is calculated from the critical wave vector $q_c = 0.0217$ Å^{-1} and absorption length 0.1016 cm^{-1}. To capture the essential features of the physical system, our real-space density profile $\rho(z)$ specifies regions for the water subphase, mineral film, arachidic acid headgroups, and hydrocarbon tails. An example profile, corresponding to the data taken 8.5 h after film compression, is shown in Figure 4a, solid line. The profile is scaled by the electron density of water (ρ_w). In the model, the densities ρ and lengths L are defined for two rectangular slabs, representing the arachidic acid tail (labeled C20) and calcium carbonate phase (CCO). The sharp rectangular slab profile is shown in Figure 4a by the short dashed line. Interfaces between the slabs are smeared by error function profiles characterized by the widths σ_0, σ_1, and σ_2 (Figure 4a, long dashed line). The final element of the model is a Gaussian term located near the interface between tails and mineral, with a variable position z_G, amplitude A_G, and width σ_G. The equation describing the full density profile is

$$\rho(z)/\rho_w = [\rho_{C20}/2]\{\mathrm{erf}[z/\sigma_0\sqrt{2}] + 1\} + [(\rho_{CCO} - \rho_{C20})/2]\{\mathrm{erf}[(z - L_{C20})/\sigma_1\sqrt{2})] + 1\} + [(1 - \rho_{CCO})/2]\{\mathrm{erf}[(z - L_{CCO} - L_{C20})/\sigma_2\sqrt{2}] + 1\} + [A_G/(\sigma_G\sqrt{2\pi})]\exp[-(z_G - z)^2/{\sigma_G}^2)] \qquad (3)$$

Since the kinematic limit is valid for $q_z \gtrsim 5q_c$, we have analyzed the data for $q_z \ge 0.1$ Å^{-1} by substituting eq 3 into eq 2. The kinematic calculation is plotted in Figure 4b as the full line, along with the experimental data (circles). This analytic calculation achieves a very good agreement between experiment and model for the chosen range of q_z, but as shown in the inset (Figure 4c), this kinematic calculation does not describe the data for low values of q_z.

At low q_z where the ratio of scattered to incident X-rays is near unity, it is necessary to make a full dynamical calculation, taking into account the multiply reflected and transmitted waves. The commonly used formalism is a numerical matrix method, which considers reflection and transmission at a series of interfaces between regions of differing electron density.[36] For this purpose, we can approximate the continuous model density profile by a digitized version which specifies the electron density $\rho(z_i)$ at discrete positions, over a range of values z_i extending well into the vapor phase (zero density) and the bulk subphase (unit density). At each of these points the electron density from the analytic model determines the index of refraction used to determine the magnitude of the scattered and transmitted waves.[37] The calculation is based upon the assumption that, for some layer sufficiently far into the sample, no intensity contributes to the reflectivity at the surface. No terms for absorption are explicitly included, however, since these would depend on the chemical composition of the scattering material, which is in our case not measured independently. In practice, absorption leads to broadening of the low-q_z peak, which is accounted for instead by the diffuse boundary parametrized by σ_2 in the model.

Points in the digitization must be close enough together to allow an accurate calculation in the desired range of q_z, without being so dense that computation time becomes prohibitive. As Figure 4a shows, we digitize our model profile in steps of 5 Å. This leads to inaccuracies at large values of q_z for two reasons. First, the fidelity to the analytic model is poor where structural features have small length scales (for example, at the Gaussian bump), and these short-range structural features manifest themselves in the reflectivity at larger q_z. A second problem is that the digitization spacing produces its own "Bragg peak" based on the digitization period. This is especially evident at large q_z values in Figure 4b, where the matrix calculation (shown by the dashed line) rises higher than the kinematic calculation by more than an order of magnitude.

Thus, our data analysis combines the kinematic calculation for $q_z > 0.1$ Å^{-1} with the matrix formalism for $q_z \le 0.1$ Å^{-1}, for a given structural model. As Figure 4b shows, the two calculations yield essentially the same results in the range $0.05 < q_z < 0.3$ Å^{-1}, differing only at the extremes. In practice, the low-q_z features depend mainly upon the parameters that define the calcium carbonate layer, ρ_{CCO}, L_{CCO}, and σ_2. The other parameters have the most effect on the reflectivity for $q_z > 0.1$ Å^{-1}. However, the final fits were arrived at by simultaneously refining both regions

(36) Gibaud, A. *X-ray and neutron reflectivity: principles and applications*; Springer: New York, 1999; Chapter 3.2.
(37) Parratt, L. G. *Phys. Rev. B* **1954**, *95*, 359.

Table 1. Parameters for the Best Fit Model Density Profiles, Defined by Eq 3

hours	ρ_{C20}/ρ_w	L_{C20} (Å)	ρ_{CCO}/ρ_w	L_{CCO} (Å)	σ_0 (Å)	σ_1 (Å)	σ_2 (Å)	A_G/ρ_w (e/Å^2)	z_G (Å)	σ_G (Å)
5.0	0.71 ± 0.05	25.2 ± 0.5	1.32 ± 0.02	71 ± 10	3.5 ± 0.2	9.6 ± 0.5	25 ± 10	2.9 ± 0.2	28 ± 10	3.6 ± 0.2
7.5	0.68 ± 0.05	25.5 ± 0.5	1.35 ± 0.02	97 ± 10	3.6 ± 0.2	10.7 ± 0.5	32 ± 10	2.7 ± 0.2	28 ± 10	3.7 ± 0.2
8.5	0.64 ± 0.05	25.4 ± 0.3	1.38 ± 0.02	130 ± 10	3.5 ± 0.2	11.2 ± 0.5	38 ± 10	2.4 ± 0.2	27 ± 10	3.7 ± 0.2
11.2	0.60 ± 0.05	24.4 ± 0.2	1.39 ± 0.02	190 ± 10	4.1 ± 0.2	11.8 ± 0.5	53 ± 10	1.8 ± 0.2	28 ± 10	3.6 ± 0.2
12.5	0.57 ± 0.05	24.3 ± 0.2	1.40 ± 0.02	227 ± 10	4.2 ± 0.2	12.4 ± 0.5	58 ± 10	1.6 ± 0.2	28 ± 10	3.6 ± 0.2
15.2	0.50 ± 0.05	24.3 ± 0.2	1.43 ± 0.02	287 ± 10	4.0 ± 0.2	13.3 ± 0.5	62 ± 10	1.5 ± 0.2	28 ± 20	3.6 ± 0.2
17.0	0.51 ± 0.05	24.3 ± 0.2	1.43 ± 0.02	296 ± 10	4.4 ± 0.2	13.1 ± 0.5	59 ± 10	1.3 ± 0.2	29 ± 20	3.4 ± 0.2
18.5	0.47 ± 0.05	24.2 ± 0.2	1.42 ± 0.02	299 ± 10	4.2 ± 0.2	13.5 ± 0.5	57 ± 10	1.2 ± 0.2	33 ± 20	3.4 ± 0.2

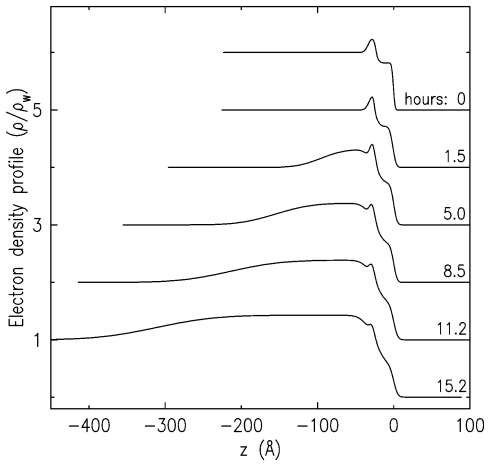

Figure 5. Time series of normalized electron density profiles obtained from fits. The region $z > 0$ is the vapor, and the sample structure is defined by regions with $z < 0$ that correspond to the hydrocarbon tails of the surfactant, a layer of headgroups and bound cations, a mineralized region with an electron density ≈1.4 times that of water, and the water subphase. (Curves are shifted for clarity.)

of the data against a single model profile. A final detail that we must note involves the effect of the finite vertical divergence of the synchrotron beam, which acts to smear out the sharp low-q_z peak. For the low-q_z region, where the matrix method was used, we also convolve the reflectivity numerically with a Gaussian function having a width of 0.001 14 Å^{-1}. This corresponds to the known vertical beam divergence of 1.4 mrad.

V. Discussion

Fits to the reflectivity data specify the densities, thicknesses, and structural details of the mineralizing system at time points separated by 2−3 h intervals. The best fit parameters are tabulated in Table 1, and correspond to the fits shown as solid lines in Figure 2. Fits shown as dashed lines in Figure 2 were obtained by fixing two of the parameters: constraining the hydrocarbon tail length $L_{C20} = 24.3$ Å, and the mineral film density $\rho_{CCO}/\rho_w = 1.43$, and these fits are of similar quality except for the few earliest data sets, where they deviate noticeably at $q_z \approx 0.07$ Å^{-1}. This shows that our measurement is very sensitive to the mineral density parametrized as ρ_{CCO}/ρ_w, and that the slight increase in this value from 1.32 to 1.43 shown in the table is a reliable observation. Representative model profiles for the full fit are shown in Figure 5. The analysis provides information about the structure at the surface at early growth times, the evolution of the mineral film, and the physical properties of the mineral film. We will now discuss these in turn, after which we will make some comments about the effects of kinetic control.

A. Film Structure at Early Times. The first model profile, describing the monolayer within an hour of being compressed to a surface pressure of 25 mN/m on the subphase, shows how the species in solution affect the structure. In comparison to the structure of arachidic acid monolayers measured previously on pure water and also on a supersaturated calcium carbonate subphase *lacking* any polymer additive,[33] the present results show a depleted density in the region of the hydrocarbon tails. The density of closely packed alkane tails is very close to that of water, and for a well-ordered monolayer we expect to find $\rho_{C20}/\rho_w \approx 0.98$.[38] In the present case by contrast, $\rho_{C20}/\rho_w \approx 0.7$. This indicates some interruption of the molecular packing, which may be due to small amounts of poly(acrylic acid) coming to the surface. We do not believe that the presence of cations in solution causes this effect. In general, cations at Langmuir films tend to have the opposite effect of increasing the surface ordering of fatty acid films,[39] and this is what we found in a previous study of arachidic acid on a supersaturated calcium carbonate solution: the molecules in that case self-assembled into a well-ordered, untilted hexagonal phase even at low surface pressure.[33]

The density in the headgroup region, defined by the Gaussian bump in the model, gives us a way to quantify the cation binding, though some assumptions must be made which will broaden the estimate. First, the excess electron density at the headgroups can be calculated by subtracting the Gaussian term from a similar fit to data obtained on a pure water subphase.[33] The measurement on pure water specifies the volume occupied by the 23 electrons contained in the COO^- group for each surfactant molecule. (At this near-neutral pH, we expect only a partial degree of deprotonation, but this does not affect the nominal electron density.) The excess electron density in this volume, for the present case, can be attributed to a mixture of Ca^{2+} ions and water. If the relative volumes of the cations and the water molecules are known, the number of bound cations per arachidic acid molecule can be obtained. Assuming that the Ca cation has a radius between 1.1 and 1.5 Å, that a water molecule occupies a radius of 1.5 Å, and that there is a full coverage of surfactant in both cases, we arrive at a cation binding of one Ca^{2+} per 20−35 arachidic acid molecules. Scaling by 70% to account for partial coverage of arachidic acid molecules (based on the electron density of the hydrocarbon tail region) changes this range to 14−25 molecules per cation. A more detailed discussion of the cation binding under a variety of conditions will be given in a forthcoming publication. For the present, we note that in this experiment the cation binding indicated by excess electron density at the monolayer is quite low: much lower than the five molecules/cation estimated for the subphase without polymer in our previous study,[33] and much too low to support a model of stoichiometric cation binding as required in the template-directed crystallization model suggested in the past.[3] One role played by the soluble polymer, evidently, is a change in the concentration of cations available to bind to the fatty acid monolayer, which

(38) Kjaer, K.; Als-Nielsen, J.; Helm, C. A.; Tippman-Krayer, P.; Möhwald, H. *J. Phys. Chem.* **1989**, *93*, 3200.
(39) Rapaport, H.; Kuzmenko, I.; Berfeld, M.; Kjaer, K.; Als-Nielsen, J.; Bopovitz-Biro, R.; Weissbuch, I.; Lahav, M.; Leiserowitz, L. *J. Phys. Chem. B* **2000**, *104*, 1399.

may be binding to the COO^- groups of the poly(acrylic acid) instead. The acidic soluble polymer thus changes both the cation binding at the charged template and the local solution chemistry near the monolayer.

Complementary information about the surface structure comes from the grazing-incidence in-plane diffraction measurement. As noted above, we can index the observed peaks in terms of a centered rectangular unit cell with lattice parameters of $a = 4.38$ Å and $b = 8.51$ Å, the average molecular area being 18.63 Å^2 per molecule. By comparison, values of 19.6−19.8 Å^2/molecule have been obtained previously for the untilted, hexagonal structure of compressed arachidic acid monolayers on pure water,[33,38] while on a supersaturated calcium carbonate subphase *lacking* polymer, the hexagonal unit cell has an area that is slightly larger (20.4 Å^2/molecule).[33] In comparison to these prior measurements, the present structure is more closely packed, and the rectangular lattice with $b/a = 1.94$ is elongated from the hexagonal cell ratio $b/a = \sqrt{3} \approx 1.73$.

The larger, hexagonal unit cells are typical of fatty acid films assembled at higher temperatures, where the chains are free to rotate relative to one another. Smaller and more elongated cells are characteristic of lattices in which the hydrocarbon backbones are ordered into herringbone[25] or pseudoherringbone[40] arrays. The 4.38 × 8.51 Å lattice observed in the present case is characteristic of the most elongated fatty acid cells reported, observed previously for behenic acid (C22) monolayers on water below room temperature.[41] This suggests a pseudoherringbone packing for the present very close-packed system, although this symmetry cannot be confirmed by the present measurements since no higher order peaks could be obtained. It is interesting that hexagonal packing is obtained either on removing the cations or on *increasing* the cation binding by removing the polymer. Whether the pseudoherringbone symmetry is obtained only for a particular range of temperature or cation binding remains to be seen. Although the fatty acid molecules are very well ordered within each domain, the 60 Å domain size we estimate from peak widths is extremely small. The disruption of the structure may be due to the presence of polymer molecules. Roughness at the mineral interface may also be a signature that the film forms by coalescence of nanoscale droplets, a growth mode of the polymer-induced liquid-precursor (PILP) process which we have observed on micron length scales by optical microscopy.[20]

Although the observed peak positions are not close to Bragg peaks of anhydrous $CaCO_3$ (calcite, vaterite, or aragonite), the first peak at 1.48 Å^{-1} is close to the (101) peak of crystalline calcium carbonate monohydrate, reported in the range 1.45−1.46 Å^{-1}.[34] The (020) and (202) peak positions for calcium carbonate hexahydrate (ikaite), at 1.52 and 1.58 Å^{-1}, respectively,[35] lie between the peaks we observe at 1.48 and 1.61 Å^{-1}. These similarities in peak position are not compelling evidence for the presence of any crystalline calcium carbonate hydrate. The peak at 1.61 Å^{-1} cannot be attributed to any mineral phase and must belong to the monolayer. Both peaks have the same width and the same q_z dependence, which constrains the interpretation that they could come from two different phases. Domain sizes would have to be the same, but more importantly, the thickness of the diffracting layers would also have to be of the same 25 Å length scale to explain the q_z dependence of scattered intensity. The mineral film, however, is hundreds of angstroms thick at late times, as the reflectivity measurements show. Therefore, the in-plane peaks do not characterize the mineral film. We attempted in this experiment to obtain the amorphous structure factor of the mineral film, but failed to identify this signal above the bulk scattering background produced by the water and the peaks produced by the surfactant. In other words, the monolayer is a very well organized volume (producing rather sharp peaks) and the water is a very large scattering volume (producing a large scattered intensity of its amorphous structure factor). Between the two, the mineral is a relatively small and disordered volume. Extracting the amorphous film for ex situ scattering measurements is an objective for future work.

B. Evolution and Characteristics of the Mineral Film. The evolution of the monolayer/mineral surface structure is outlined in Figure 5, which shows selected model density profiles from the initial film structure to the final structure. Each profile shows features identifiable as the hydrocarbon tails, the headgroup region, and, at later times, the mineral film. The arachidic acid features become more disrupted as time progresses, although they remain clearly seen. Models in which the headgroup and tail features were removed or made less well-defined than what is shown were attempted, but such fits did not describe the data. Similarly, the in-plane peaks show little time dependence. We conclude that the monolayer film, though considerably disordered, remains in place while the system mineralizes.

The mineral film has an electron density at early times of 1.32 ± 0.02 times that of water, which increases over the course of 10 h to a maximum value of $1.43\rho_w$, or 1.43 × 0.334 electrons/Å^3 = 0.48 electron/Å^3 (Table 1). By comparison, the electron densities of the anhydrous crystalline $CaCO_3$ phases lie in the range 0.80−0.89 electron/Å^3, nearly twice as dense.[42] The density we observe is much closer to that of $CaCO_3 \cdot 6H_2O$, which is 0.57 electron/Å^3. Given its density of about 70% that of the hexahydrate, and the lack of sharp diffraction peaks, we conclude that the mineral film is a hydrated, amorphous phase with an open structure. The 8% increase in density observed in the first few hours may then be due to partial dehydration. The amorphous character persisted until the end of the experiment, 20 h after film preparation, at which time the film was solid and thick enough to lift out of the water onto a glass coverslip. Examination of the air-dried film by polarized light microscopy showed a smooth and glassy texture, with cracks running in apparently random directions. The film is dotted with birefringent rhombohedral crystals on the order of 10 μm in size (covering less than 1% of the surface). A number of such crystals typically can be seen by eye, reflecting glints of light at the liquid surface during the later stages of our experiments. We believe that homogeneous nucleation of calcite in solution always occurs to some extent, and that some of these crystals find their way to the surface, especially if the surfactant coverage is disrupted. Therefore, these calcite crystals probably do not represent crystallized regions of the surfactant-nucleated film. It is not clear from the present experiment how crystallization and dehydration would have proceeded had the film remained longer in the water—further studies are underway.

From the model fits, we have determined the thickness of the mineral film (given by the parameter L_{CCO}) as a function of time, and this is plotted in Figure 6. Regardless

(40) Kuzmenko, I.; Kaganer, V. M.; Leiserowitz, L. *Langmuir* **1998**, *14*, 3882.

(41) Kenn, R. M.; Böhm, C.; Bibo, A. M.; Peterson, I. R.; Möhwald, H.; Als-Nielsen, J.; Kjaer, K. *J. Phys. Chem.* **1991**, *95*, 2092.

(42) Weast, R. C., Ed. *CRC Handbook of Chemistry and Physics*; CRC Press: Boca Raton, FL, 1985.

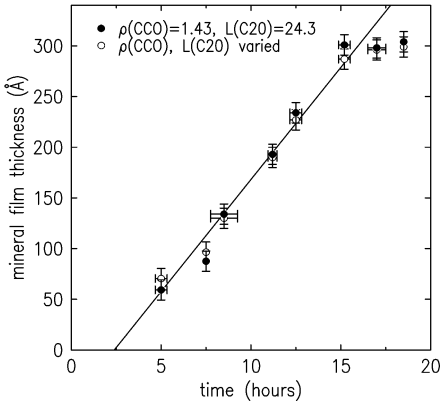

Figure 6. (○) Mineral film thickness extracted from fit parameter L_{CCO}, as a function of time from the preparation and compression of the arachidic acid monolayer, with parameters as given in Table 1. (●) Results obtained with mineral electron density ρ_{CCO} fixed at $1.43\rho_w$ and hydrocarbon tail length fixed at 24.3 Å. Horizontal error bars indicate the amount of time needed to acquire the reflectivity data at each point; vertical error bars show the statistical variation of the parameter within the context of the given fit. The line is fit to points for times up to and including 15 h.

of whether the parameters ρ_{CCO} and L_{C20} are allowed to vary, we find essentially the same results. The thickness observed for the three latest data points is limited by the experimental resolution. The line is fit to all data points excepting the last two, and indicates an intercept or "induction time" of 2.5 h and a growth rate of 22 Å/h. We believe that this is the first time that microscopic nucleation parameters have been directly measured at early growth times for such a mineralizing system. Further work is underway by our group to characterize these kinetic parameters as functions of polymer additive (species, molecular weight, and concentration) and other physical parameters. Our in situ technique should allow us to make great strides in clarifying the mechanisms by which such inhibitors affect mineralization at smooth organic templates. At the moment, the most obvious mechanism to suggest is that the COO^- groups of the polymer have removed cations from solution, as evident from the reduction in cation binding at the monolayer relative to solutions that lack the polymer.[33]

At the same time, we must add a word of caution about a very important and weakly controlled variable, which is the rate of diffusion of CO_2 gas from the liquid. The CO_2 evaporation, which increases the $CaCO_3$ supersaturation near the monolayer as a function of time, is in fact the most significant kinetic factor in this experiment. We found in subsequent studies, for example, that by reducing the depth of the water from 8 to 2 mm, the film growth occurs 5 times faster for the same chemical conditions. What is more, for this latter condition the film never stabilizes, but instead dissolves again within 12 h. (Possibly the instability may be related to the change in pH that accompanies the gas escape, and we intend to clarify this in future work.) For other studies in the literature, in which characterization of a solid end product is required to tell the story, the nonmineralizing regimes of calcium carbonate subphase systems tend to go unreported.[19,22,43] For our measurements, where structures at early growth times can be detected even when they are ultimately unstable, even the experiments that do not make films or crystals will provide us with information on how the template structure and the species in solution work together to determine the routes through which mineralization can proceed. The present experiments suggest to us that fatty acid films do not play a strong part as structural templates for calcium carbonates. Observations from our other studies, however, suggest a very important role for the template with respect to where the precursor phase is deposited, and in modulating the transformation/crystallization of the amorphous precursor phase.[30] We look forward to further experiments which can clarify the role of macromolecular template and solution kinetics in similar systems.

VI. Summary

The nucleation and growth of a biomimetic mineral film at a Langmuir monolayer interface has been observed in situ with synchrotron X-ray scattering. We have measured the induction time and growth rate of a calcium carbonate film, nucleating at a fatty acid monolayer from a supersaturated calcium carbonate subphase containing a dilute poly(acrylic acid) additive mimicking the acidic proteins found in biomineralizing systems. The arachidic acid molecules were observed to self-assemble on the subphase into an untilted centered rectangular unit cell, with an in-plane area of 18.6 $Å^2$/molecule, and one bound Ca^{2+} ion per 14−25 surfactant molecules. Subsequently, an amorphous mineral phase was observed, growing at a rate of 22 Å/h to a thickness of 300 Å after about 15 h. The electron density of the film was 0.7 times that of crystalline calcium carbonate hexahydrate, suggesting that the precursor is a hydrated phase with an open structure. During film growth, no changes were observed in the in-plane scattering peaks from the arachidic acid monolayer. No intensity was observed at Bragg peak positions for anhydrous calcium carbonate minerals. Our observations indicate that nucleation of the calcium carbonate film is not directed by atomic-scale templating at the fatty acid, but is instead dictated by chemical species localized near the monolayer. The rate of CO_2 gas escape and the concentration and molecular weight of the polymer additive determine the kinetics and control mineralization in this system.

Acknowledgment. We thank Masa Fukuto and Oleg Shpyrko of Harvard University for helpful discussions of the matrix formalism. L.B.G. acknowledges support from NSF CAREER Grant DMR-0094209 and the National Institutes of Health (DK59765-01). The National Synchrotron Light Source is supported under U.S. DOE Contract No. DE-AC02-98CH10886.

LA0260032

(43) Lahiri, J.; Xu, G.; Dabbs, D. M.; Yao, N.; Aksay, I. A.; Groves, J. T. *J. Am. Chem. Soc.* **1997**, *119*, 9.